# Diagnosing Ocean Unstable Baroclinic Waves and Meanders Using the Quasigeostrophic Equations and Q-Vector Method

JIA WANG

*Rosenstiel School of Marine and Atmospheric Science, University of Miami, Miami, Florida*

MOTO IKEDA

*Graduate School of Environmental Earth Science, Hokkaido University, Sapporo, Japan*

27 April 1995 and 22 November 1996

ABSTRACT

A three-dimensional, primitive equation model is applied to the ocean mesoscale eddies and unstable baroclinic waves across a density front in a channel under a very low viscosity environment. Current meanders are well produced. The unstable baroclinic waves are examined for flat, positive (same sense as isopycnal tilt) and negative sloping bottoms. The growth rates with flat, gentle, medium, and steep slopes and with different wavelengths (wavenumbers) are discussed. A positive slope clearly suppresses the meandering wave growth rate whose maximum slightly shifts to a lower wavenumber compared to the flat bottom. A gentle negative slope, however, favors the wave growth with the maximum shifting toward higher wavenumber. When the negative slope becomes steeper, the growth rate significantly decreases correspondingly.

Furthermore, a diagnostic analysis package for the pressure tendency and vertical velocity equations, analogous to the approaches in meteorology ($\omega$ equation and Q-vector method), is developed for the first time to reveal the physical processes and mechanisms of the unstable wave propagation in the midlatitude ocean. The weaknesses and strengths of these two diagnostic approaches are evaluated and compared to the model results. The Q-vector method is superior to the quasigeostrophic $\omega$ equation for diagnosing the vertical motion associated with the mesoscale dynamics from a hydrographic CTD array because the former has no phase error.

## 1. Introduction

Meanders and mesoscale eddies are a ubiquitous feature of ocean currents, for example, along the Kuroshio, the Gulf Stream, the Florida Current (Lee and Mayer 1977), and the Labrador Current (LeBlond 1982; Ikeda 1991), etc. The measurements of surface trajectories of the Gulf Stream and its induced warm and cold rings (mesoscale eddies) were taken by Richardson (1981), Vastano et al. (1980), and Joyce (1984). The lifetime of these mesoscale eddies ranges from weeks to months.

Measurements of Gulf Stream meanders using a Lagrangian isopycnal float made it possible to track the paths of the fluid parcels and the rising and descending motions associated with mesoscale eddies (Bower and Rossby 1989). The progress led to using a meteorological approach, a quasigeostrophic (QG) vorticity equation (Holton 1979), to calculate the vertical velocity (Lindstrom and Watts 1994). Lindstrom and Watts found that upwelling (downwelling) occurred from trough (crest) to crest (trough) of a meandering wave, consistent with the results in a developing synoptic baroclinic wave (cyclone or anticyclone) in the atmosphere. Vertical motion across an ocean front and the associated mesoscale features were determined from hydrographic CTD (conductivity–temperature–depth) data using the meteorological approach, the Q-vector method (Hoskins et al. 1978), by Leach (1987), Tintoré et al. (1991), and Pollard and Regier (1992).

Mesoscale eddies have been reproduced using a QG model (Holland 1978; Ikeda 1981; Ikeda and Apel 1981; Ikeda 1991) to examine the generation mechanism in an idealized ocean basin. The mesoscale eddy generation and development are associated with baroclinic instability, and they decay because of eddy viscosity dissipation and interactions with the mean flow. To include as much physics as possible, many efforts have been made in using the primitive equation (PE) models to examine baroclinic instability (Orlanski and Cox 1973; Wood 1988; Oey 1988; Chao 1990; Spall and Robinson 1990; Ikeda and Zhang 1992; Ikeda and Wood 1993; Wood and Ikeda 1994). Most of the PE models were based on the Cox–Bryan model (Cox 1984) with the rigid-lid approximation and the B grid. Killworth et al.

*Corresponding author address:* Dr. Jia Wang, Ocean Pollution Research Center, Rosentiel School of Marine and Atmospheric Science, University of Miami, 4600 Rickenbacker Causeway, Miami, FL 33149.
E-mail: jia.wang@.rsmas.miami.edu

(1984) analytically and numerically examined wave propagation and growth rate on a surface front in a two-layer geostrophic current. They found that the growth rate is sensitive to the ocean depth.

Although some diagnostic equations, such as the Q-vector method (Leach 1987; Tintoré et al. 1991; Pollard and Regier 1992) and $\omega$ equation (Lindstrom and Watts 1994), have been applied to hydrographic CTD data to estimate the vertical motion, there was no comparison between these two methods in the ocean. Thus, our major motivation is to develop robust diagnostic equations, analogous to the meteorological approach, to analyze the mesoscale features simulated in a 3D primitive equation model and to evaluate the weaknesses and strengths of the two methods. The final goal is to provide a diagnostic tool to the oceanographic community to digest hydrographic CTD data in the ocean and 3D model products.

To achieve this goal, we need to use a 3D primitive equation model with free surface and the sigma coordinate in the vertical. The model then provides a 3D time-dependent density field to the diagnostic equations. We will modify and apply ECOMSI (Estuarine and Coastal Ocean Model with a Semi-Implicit scheme, Blumberg 1991) to accurately produce some mesoscale features and dynamic processes with analogous characteristics to the atmospheric synoptic baroclinic wave. Furthermore, the eddy growth rate versus wavenumber for different wavelengths and different slopes will be generated. The effects of sloping bottoms on growth of baroclinic waves will be discussed as well.

The description of the ECOMSI and the modification are given in section 2. In section 3, the model's capability is shown by presenting the growth rate in both flat and sloping bottom channels. In section 4, the diagnostic equations for pressure tendency and vertical velocity, as well as the Q-vector approach, are derived and applied to interpret mesoscale features. The summary and conclusions are given in section 5.

## 2. Description of the model and boundary conditions

### *a. Description of the model*

Details of the Princeton Ocean Model (POM) were given in Mellor (1991). That version of the model uses a leapfrog scheme in time and mode-splitting techniques for slowly moving waves (internal mode) and fast-moving waves (surface gravity waves, external mode) with the latter obeying the Courant–Friedrichs–Lewy (CFL) criterion. As a result, a filter (Asselin 1972) in the time domain has to be used every time step to remove computational modes produced by the leapfrog scheme. A version of the model was rewritten and named ECOMSI (Blumberg 1991), which has the following features: 1) horizontal curvilinear coordinates and the Arakawa C grid, 2) sigma coordinates in the vertical with realistic bathymetry, 3) a free surface, 4) a second-order turbulence closure model for the vertical viscosity (Mellor and Yamada 1982), 5) horizontal diffusivity coefficients calculated by the Smagorinsky (1963) parameterization (these features 1 through 5 were preserved from POM), 6) a semi-implicit scheme used to calculate the surface elevation in the shallow-water equations with the stringent CFL criterion removed (Casulli and Cheng 1992; Wang et al. 1994), and 7) an Euler forward scheme in time used for all equations. Because of the Euler forward time scheme used in the ECOMSI compared to the leapfrog time scheme used in POM, the mode-splitting technique and Asselin filtering every time step have been abandoned. However, because of the Euler forward scheme in time, an inertial instability occurs. Yet, in order to stabilize the model, a sufficient large viscosity has to be used. Thus, we introduce a third version of this model using a predictor–corrector scheme to overcome the inertial instability (Wang and Ikeda 1995, 1997, hereafter WI97).

It must be pointed out that the pure advection scheme (even with a conservative flux form) of ECOMSI in the absence of dissipation is still a weakly unstable scheme with the amplification factor, or the eigenvalue, being $|\lambda| = 1 + O(\Delta t^2) > 1$. However, the overall numerical schemes for the advection–diffusion equations are conditionally stable if the Courant number is less than 1/3 and $A_H\Delta t/\Delta s^2$ is less than 1/6 (Roache 1976, chap. 3), where $A_H$ is horizontal eddy viscosity, $\Delta s = \Delta x = \Delta y$ is the grid spacing, and $\Delta$t is the integration time step. It should be kept in mind that the numerical schemes are of *first-order accuracy* in time and second-order accuracy in space. Therefore, the advection scheme here introduces a negative artificial viscosity (Roache 1976), which can be cancelled by adding the same quantity in the finite-difference equations.

### *b. Model configuration*

The model ocean is a zonal channel with two open boundaries on the eastern and western sides where a cyclic boundary condition is applied to all variables that are prognostically computed. A rectangular channel 112 km wide was used. The length of the channel varied as we simulated the instability of the different wavelengths. The model resolution is 5.559 km $\times$ 5.559 km, less than half the internal Rossby radius of deformation, $R_d = (g'd)^{1/2}/f$, where $g' = g(\rho_2 - \rho_1)/\rho_2$ is the reduced gravity acceleration, $(\rho_1, \rho_2) = (1026.69, 1027.75)$ kg m$^{-3}$ for the values of the upper and lower layers, respectively, and $d = 160$ m is the vertical scale of the front. With $g = 9.8$ m s$^{-2}$ and $f = 10^{-4}$ s$^{-1}$, $R_d$ is estimated to be about 12.7 km. Thus, the model grid is eddy-resolving. There are 21 vertical $\sigma$ levels (0.0, $-.04$, $-.08$, $-.115$, $-.15$, $-.185$, $-.22$, $-.255$, $-.29$, $-.33$, $-.40$, $-.47$, $-.54$, $-.61$, $-.68$, $-.75$, $-.80$, $-.85$, $-.90$, $-.95$, $-1.0$). To minimize the computa-

tional requirements, we set the average water depth to be 1000 m. This may have an effect on the growth rate of the wave, as Killworth et al. (1984) stated, because the front is placed between 100 and 300 m. They found, using a surface front in a two-layer geostrophic model, that the growth rate is sensitive to the fluid depth when baroclinic instability is possible. Although the configuration here is mainly applied to the Straits of Florida and the Labrador shelf, the results obtained in this paper also provide physical insight into the Gulf Stream and the Kuroshio over the continental shelf.

The initial temperature ($T$) and salinity ($S$) were used to calculate the density ($\rho$) using the equation of state (Fofonoff 1962). Then, using the density, the geostrophic velocity [$U(y,z)$] was computed. Having known $\rho$ and $U$, the initial profile (position) of the front is defined as

$$h(y) = H_0 - \frac{U_0 f}{g'} \int_{y_0}^{y} \exp\left\{-\left(\frac{y - y_0}{a}\right)^2\right\} dy, \quad (1)$$

where $h(y)$ is the depth of the front, $y_0$ is the location of the front, $H_0$ is the mean depth of the front, $U_0$ is the maximum speed of the current associated with the front, $f$ is the Coriolis force, and $a$ is the width of the front and equals to $1.8R_d = 28.86$ km. Thus, the cross-channel isopycnal tilt or slope of the front is $(\rho_2 - \rho_1)/1.8R_d = 1.06/(28.8 \times 10^3) = 3.673 \times 10^{-5}$ (kg m$^{-3}$) m$^{-1}$. We chose $H_0 = 200$ m, $y_0$ to be the center of the channel, and $U_0 = 0.3$ m s$^{-1}$. The vertical profiles of density and velocity across the front (along a south to north section), the plan views of velocity superimposed by density, and surface elevation are illustrated in Fig. 1. The salinity and temperature field (thus the density) have been disturbed in the upper 220 m with a sinusoidal perturbation having a wavelength same as the channel length $L_x$. The form of the perturbation is given as

$$0.1 \sin\left(\frac{2\pi}{L_x}x\right) \exp\left[-\left(\frac{y - y_0}{a}\right)^2\right]. \quad (2)$$

The perturbation is introduced to speed up the development of unstable waves. The initial geostrophic flow is calculated based on the geostrophic balance using the density field (derived from $T$ and $S$ fields), as described above (Fig. 1b).

The waves, having a wavenumber that is a multiple of $2\pi/K_x$, are able to grow in this configuration because of the cyclic (periodic) boundary conditions. Note that the periodic boundary condition excludes the spatial growing meanders (Ikeda 1981). The model is run with the initial conditions shown in Fig. 1. The linear growth rates are determined for channels of different lengths (different wavelengths), for the flat bottom (1000 m), and for different (positive or negative) topographic slopes across the channel. A topographic slope tilted in the same direction as the frontal slope is defined as a positive slope, and the other in the opposite sign is defined as a negative slope. The negative slope configuration mimics the front off the Labrador Shelf, while the positive slope is similar to the Florida Current and also to the Gulf Stream along the continental slope of the eastern United States.

To simplify the discussion, we set constant effective horizontal eddy viscosity and diffusivity to be 50 and 10 m$^2$ s$^{-1}$, and constant vertical eddy viscosity and diffusivity to be $10^{-4}$ m$^2$ s$^{-1}$ for all runs. The time step is 120 s, which is six times the CFL condition (Wang 1996) because the semi-implicit scheme is used. The model was integrated to 40 or 60 days for each case.

## 3. Simulation results

### *a. Energies derived from ECOMSI and the P–C version*

Total kinetic energy (TKE), zonal mean kinetic energy (ZKE), eddy kinetic energy (EKE), equivalent available potential energy (APE), and the vertical component of potential vorticity (PV) were computed. We see that ECOMSI gives growing inertial oscillations (Fig. 2a), which is the so-called inertial instability, as discussed by Wang and Ikeda (1995, WI97). As a result, the average growth rate (EKE) is 10% larger than that derived from the predictor–corrector (P–C) version (Fig. 2b). This increase in EKE may result from the interaction between mesoscale eddies and the unstable inertial oscillation. After modifying ECOMSI by introducing the predictor–corrector scheme, the growth rate is fairly well determined without any inertial instability (Fig. 2b) because the inertial oscillation gradually dies out due to weak dissipation. Thus, the P–C version of the model is more suitable than the original version for simulating mesoscale eddies under the low viscosity environment.

The initial APE slowly declines before day 20. As EKE rapidly increases and extracts energy from APE, APE correspondingly decreases. At about day 38, EKE reaches the maximum, while APE has a maximum depleting rate. TKE + APE gradually decreases with a small rise at day 34. After day 30, TKE becomes larger than APE since APE is gradually depleted.

### *b. Unstable waves and meanders in the flat-bottom ocean*

Evolution of a meander in terms of sigma-t, PV, surface height, and vertical velocity fields at depth 200 m for days 20, 30, and 40 is shown in Fig. 3. A meander starts developing from day 20, with downstream propagation to the east. The wave has its trough, ridge, and trough in the center of the domain at days 20, 30, and 40, respectively (Fig. 3c), based on the surface height fields. This can be seen from velocity and density (Fig. 3a) and PV (Fig. 3b) fields during the same period.

Propagating signals from the vertical velocity field are plausible (Fig. 3d). The simulated downstream propagating wave was estimated to travel at a speed of about

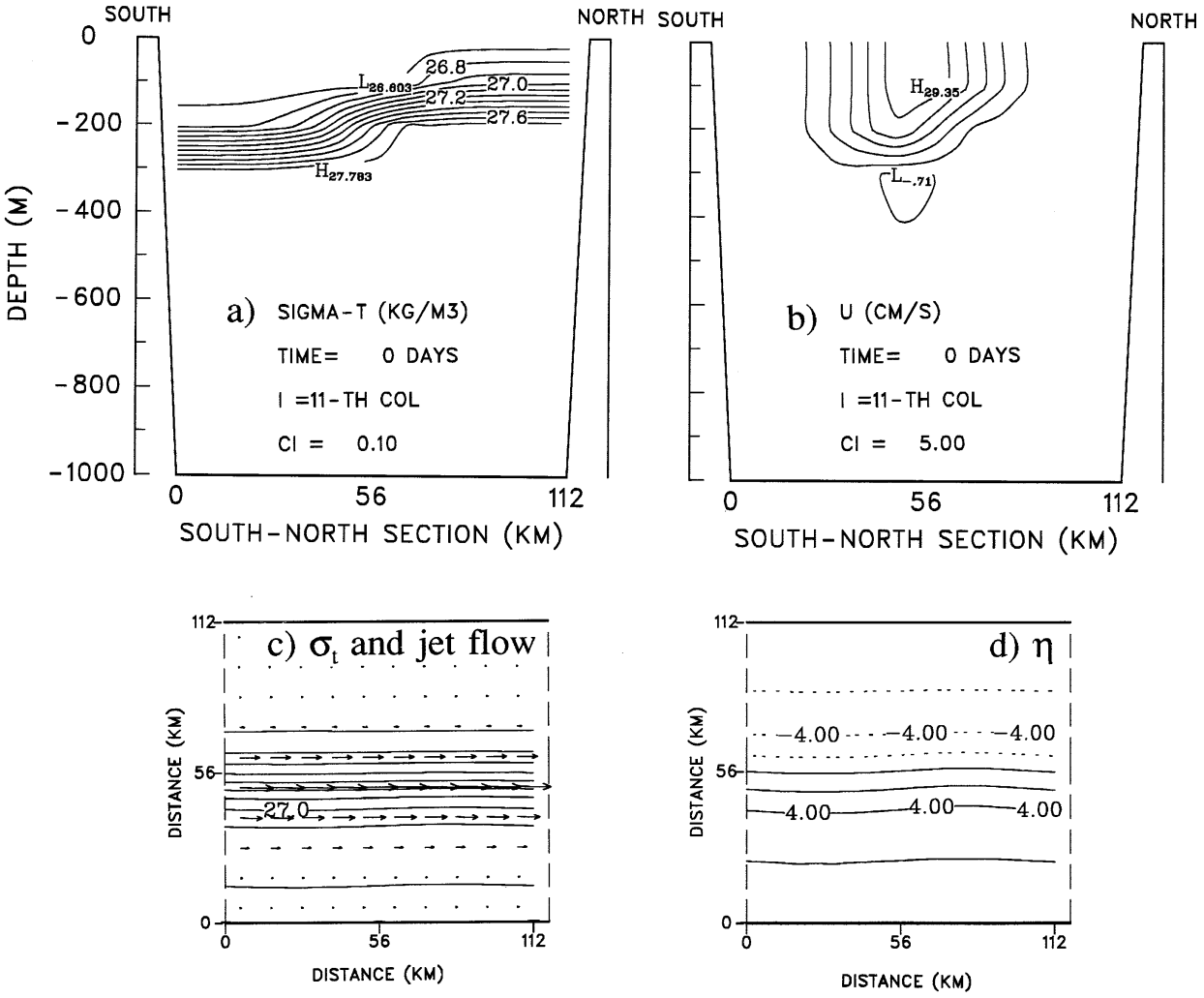


FIG. 1. South-to-north vertical structures of initial sigma-t (a), eastward jet (geostrophic) flow (b), plan view of initial 200-m sigma-t (in kg $m^{-3}$) superimposed by the zonal jet (c, with maximum velocity vector being 0.3 m $s^{-1}$), and surface height (d, in cm). The contour intervals are 0.1 kg $m^{-3}$ and 2 cm, respectively, for sigma-*t* (c) and surface height (d).

6.5 cm $s^{-1}$ from west to east. The magnitude of the vertical velocity is about 0.01 cm $s^{-1}$ or 8.64 m $day^{-1}$. An interesting phenomenon to note is that to the west (east) of the ridge, upwelling (downwelling) occurs simultaneously during the developing phase (at days 20 and 30). However, during the mature or decaying phase (day 40), the upwelling (downwelling) occurs at the wave ridge (trough). These are the features of baroclinic waves observed in the atmosphere, which were theoretically explained using the tendency and omega equations by Holton (1979, chap. 7). To apply the theory to the ocean, we will similarly interpret these phenomena observed from our numerical model output in section 4.

One striking feature in Fig. 4 is that the velocity profiles at days 30 and 40 have a tilt from bottom to surface (as shown by the thick lines), showing these profiles to be about 90° out of phase with the lower layer wave leading the upper. This feature with vertical shear indicates propagation of typical, unstable baroclinic waves in the ocean, analogous to those observed in the atmosphere (Holton 1979, chap. 7; Gill 1982, chap. 13), although no observation of such a tilt was reported in the ocean (Bower and Rossby 1989; Lindstrom and Watts 1994). However, the model results have shown this type of shift using a linear analytical model (e.g., Killworth et al. 1984) and numerical models (e.g., Wood and Ikeda 1994).

### *c. Effect of positive/negative slope and linear growth rates*

To examine the effect of slopes on unstable baroclinic waves, we introduced two types of slopes with the average depth being the same as in the flat-bottom case (1000 m). The positive slope has the same orientation (slope) as the front. For example, the bottom of a gentle

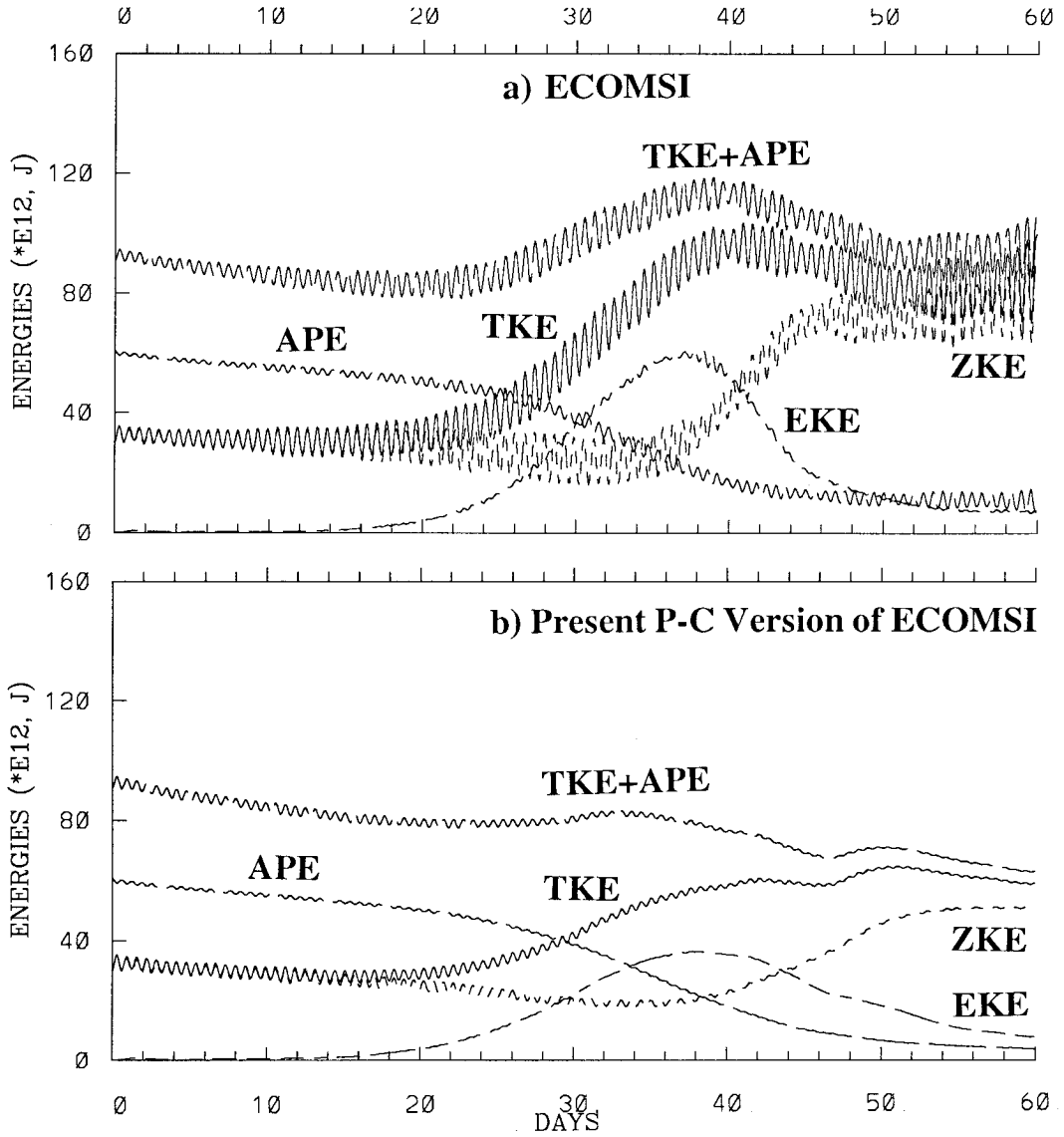


FIG. 2. Time sequences of TKE, ZKE, and EKE derived from (a) ECOMSI and (b) from the present P–C version of the model.

positive slope is defined such that it is deeper by 75 m (i.e., 1075 m) in the southern boundary and shallower by 75 m (i.e., 925 m) in the northern boundary than the average depth (1000 m). The negative slope has the opposite orientation to the positive one. Note that the positive slope has a physical setting similar to the Florida Current and the Gulf Stream along the east continental slope and the negative slope mimics the Labrador Current.

The spatial variations from these two cases at day 40 are discussed (Fig. 5). The gentle positive slope stabilizes the flow, hindering unstable waves from developing (Fig. 5a). On the contrary, well-developed waves are seen for the gentle negative slope (Fig. 5b). Particularly, a cyclonic ring (or eddy) starts to detach (pinch off) to the southeast from the main stream. At the same time, an anticyclonic eddy is generated. These eddies would eventually be expected to cut off from its parent main stream (Ikeda 1981) if the width of the channel in this study were extended to a certain distance so that the southern and northern boundaries had little effect on the development of eddies. This topic will be carried out in another study to examine the detached eddies and the nonlinear effect.

To systematically examine the wave growth versus different wavelengths or wavenumbers and the effect of topography on growing waves, a series of runs with different wavelength channels and different slopes were carried out. The average linear growth rate of the meandering wave was determined from the quantity

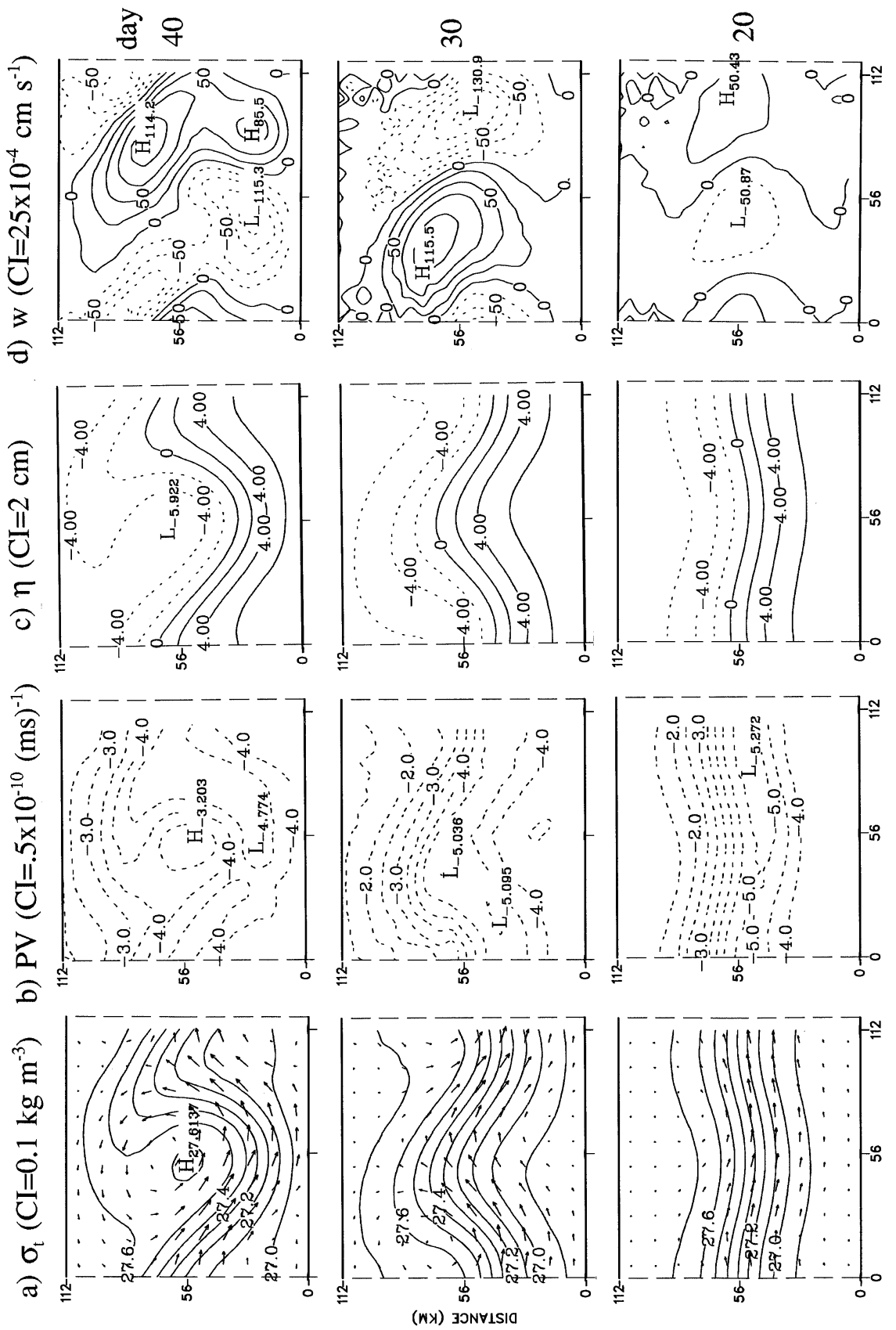


FIG. 3. Plan view of time sequences (days 20, 30, and 40) of 200-m sigma-t superimposed by the (a) velocity vectors, (b) potential vorticity, (c) surface height, and (d) vertical velocity.

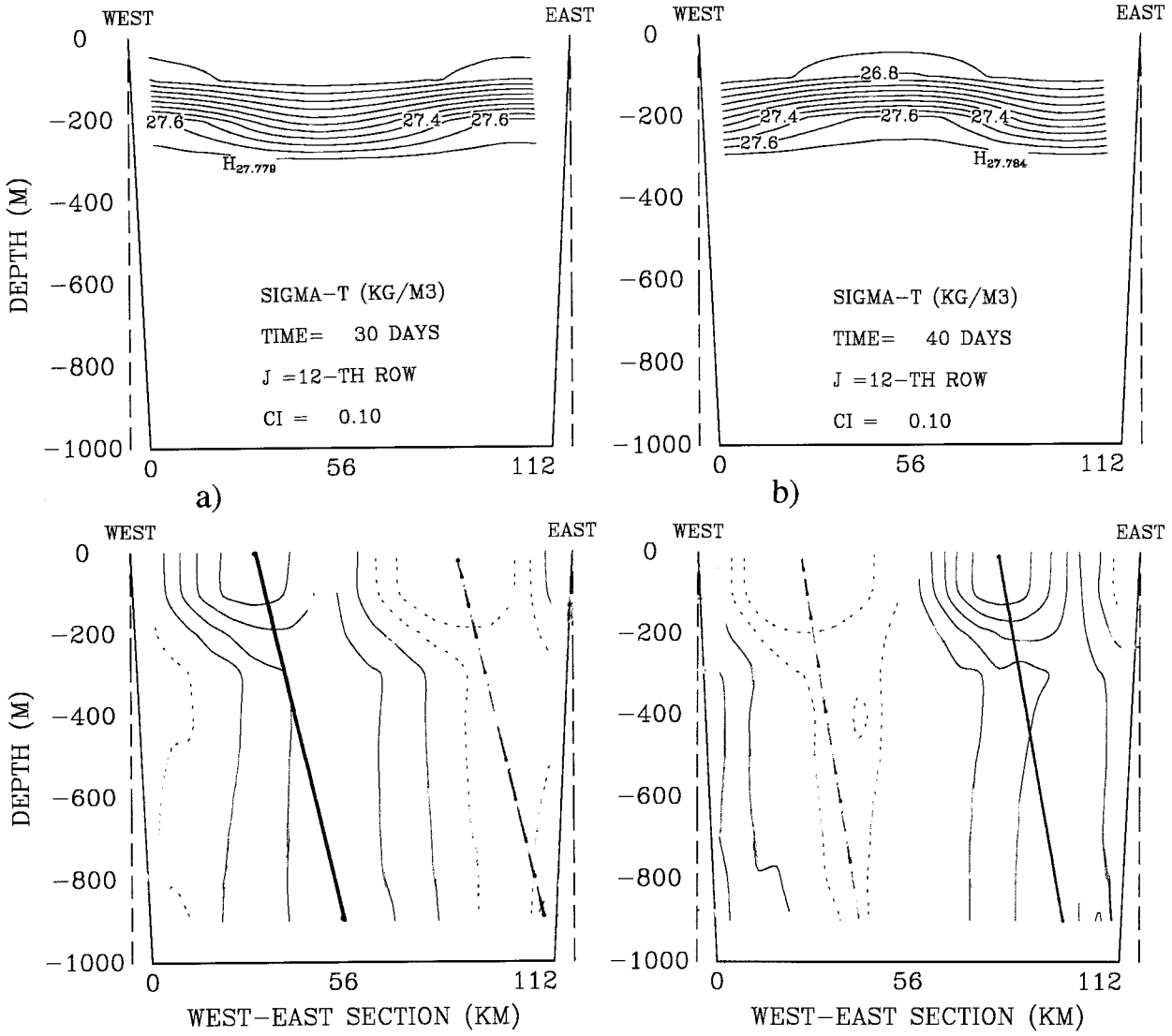


FIG. 4. West-to-east vertical structures of sigma-t (upper panels) and north–south (V) component (lower panels with contour interval being 5 cm $s^{-1}$) for (a) day 30 and (b) day 40 in a channel of 112-km width. The solid (dashed) curves indicate the northward (southward) flow. The thick solid (dashed) lines denote the ridge (trough) lines between upper- and lower-layer waves.

$[\partial \ln (\mathrm{EKE})/\partial t]/2$. The average linear growth rate was taken from the period during which this quantity is almost constant. Three types of slopes were introduced for both positive and negative sloping bottoms. The gentle slope is defined as before, that is, the depth difference between the northern and southern boundaries is $\Delta H =$ 150 m; the medium slope has the depth difference of $\Delta H = 250$ m; and the steep slope has the difference of $\Delta H = 500$ m. Thus, the cross-channel topographic gradients or slopes of the gentle, medium, and steep slopes are $1.339 \times 10^{-3}$, $2.232 \times 10^{-3}$, and $4.464 \times 10^{-3}$, respectively. A series of runs with different wavelength channels, from 68 to 178 km, for all six types of slopes plus the flat bottom, were conducted.

Figure 6 shows growth rates for both positive and negative slopes with comparison to the flat-bottom case. From the flat-bottom case, we see that the maximum growth rate peaks between wavenumbers 4 and 5 ($10^{-2}$ $km^{-1}$). The cutoff wavenumber (the zero growth rate) is 7 ($10^{-2}$ $km^{-1}$).

Once the negative slope is implemented into the model, the maximum growth rate shifts to a higher wavenumber for the gentle slope (−150 m). For the medium slope (−250 m), the growth rate is similar to the gentle slope case, indicating that the instability is not sensitive to these two slopes. A possible explanation may be that both slopes belong to a similar unstable region that was also found in the isopycnal model (Griffiths et al. 1997). However, a steep slope (−500 m) significantly suppresses the wave growth rate that also shifts further toward the higher wavenumber, with the maximum peaking between wavenumbers 8 and 9 ($10^{-2}$ $km^{-1}$).

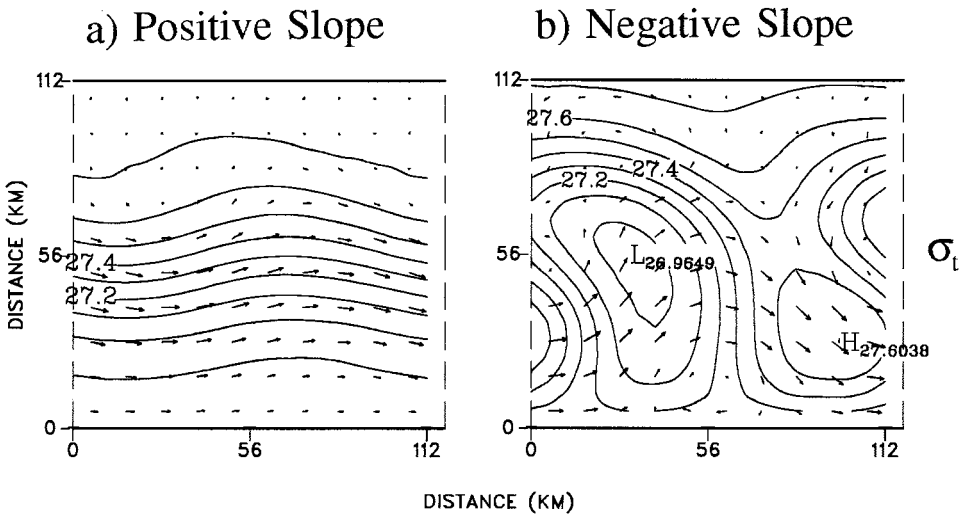


FIG. 5. Plan view of 200-m sigma-t ($\sigma_t$) superimposed by the velocity vectors at day 40 for the (a) gentle positive slope ocean and (b) gentle negative slope ocean. Contour intervals as in Fig. 2.

This result implies that the shorter mesoscale eddies tend to be active in the Labrador Current off the Labrador shelves (LeBlond 1982; Ikeda 1991).

More strikingly, an introduction of the gentle positive slope (+150 m) significantly suppresses the growth rate of the baroclinic wave. In contrast to the negative slopes, the general growth rate shifts slightly from the high wavenumber toward the lower wavenumber (longer wavelength) for the gentle positive slope, with the maximum growth rate remaining the same wavenumber. However, the growth rates are significantly reduced compared to the flat-bottom case. The growth rates for the medium (+250 m) and steep (+500 m) positive slopes are zero, indicating that the positive slope, like the Florida Current passing the Straits of Florida, significantly suppresses mesoscale meandering waves. This is true for the Gulf Stream along the east continental shelf of North America. This result is consistent with that by Boudra et al. (1988). Using an isopycnal coordinate model, they found that an introduction of the realistic topography at 27°N of the Straits of Florida to the model significantly reduces the meandering wave.

## 4. Diagnostic analysis: Pressure tendency and vertical velocity equations

To diagnose the vorticity balance of baroclinic waves associated with vertical rising and sinking motions as discussed in section 3a (Fig. 3d), we develop the diagnostic pressure tendency and vertical velocity equations to examine the physical mechanism maintaining the propagating unstable wave in terms of vorticity dy-

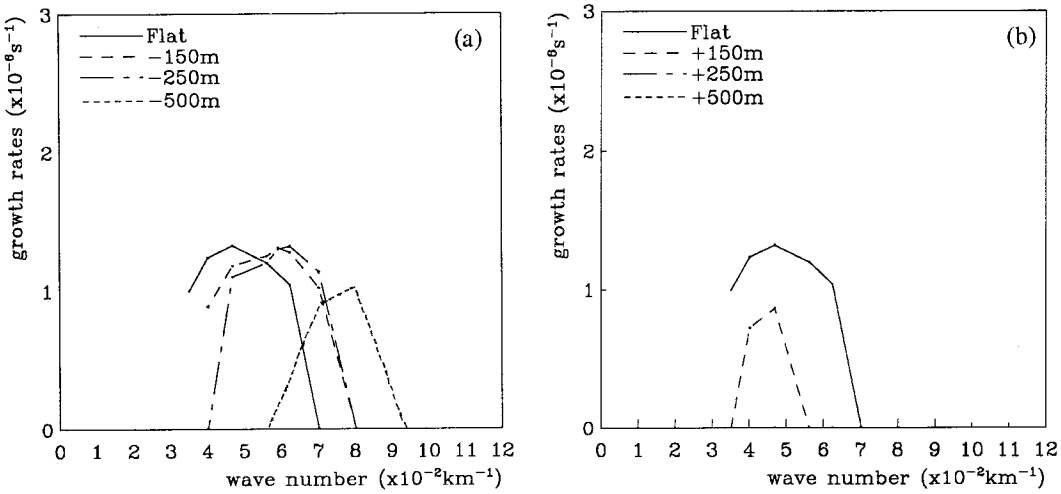


FIG. 6. The linear growth rates versus wavenumbers, $k_x = 2\pi/L_x$, for the flat-bottom channel (solid curves), and for the channels with (a) negative and (b) positive slopes.

namics. By using a similar idea of the $\omega$ equation and geopotential tendency in the isobaric coordinate system as in Holton (1979), we directly develop the $w$ equation and pressure tendency equation in a Cartesian coordinate system for the sake of convenience. In terms of the three-dimensional model, it is advantageous to calculate all the variables in the model grids.

### *a. Quasigeostrophic approach*

The Boussinesq and hydrostatic approximations still hold as in the primitive equation model; we further neglect all the dissipation terms except that the density equation is directly used. Through some algebraic operations (cf. Holton 1979), the pressure tendency ($\chi = \partial p/\partial t$) and the vertical velocity equations can be derived as follows:

$$\underbrace{\left(\nabla^2 + \frac{f_0^2}{N^2}\frac{\partial^2}{\partial z^2}\right)\chi}_{\text{PA}} = \underbrace{-\rho_0 f_0 \mathbf{V}_g\cdot\boldsymbol{\nabla}\left(\frac{\nabla^2 p}{\rho_0 f_0} + f\right)}_{\text{PB}} + \underbrace{\frac{f_0^2}{N^2}\frac{\partial}{\partial z}\left(-\mathbf{V}_g\cdot\boldsymbol{\nabla}\frac{\partial p}{\partial z}\right)}_{\text{PC}} \tag{3}$$

and

$$\underbrace{\left(\nabla^2 + \frac{f_0^2}{N^2}\frac{\partial^2}{\partial z^2}\right)w}_{\text{WA}} = \underbrace{\frac{f_0}{N^2}\frac{\partial}{\partial z}\left[\mathbf{V}_g\cdot\boldsymbol{\nabla}\left(\frac{\nabla^2 p}{\rho_0 f_0} + f\right)\right]}_{\text{WB}} + \underbrace{\frac{1}{\rho_0 N^2}\nabla^2\left(-\mathbf{V}_g\cdot\boldsymbol{\nabla}\frac{\partial p}{\partial z}\right)}_{\text{WC}}. \tag{4}$$

Physical interpretation of the above two equations is as follows: Terms PA and WA involve only second-order derivatives in space of the $\chi$ and $w$ fields. For wavelike disturbances, these two terms can be shown to be proportional to $-\chi$ and $-w$, respectively. Similarly, since it was observed that the midlatitude mesoscale eddies and meanders generally have a vertical scale comparable to the water depth H (Vastano et al. 1980; Joyce 1984), we can crudely approximate the vertical variations of $\chi$ and $w$ by letting $\partial^2(\chi, w)/\partial z^2 \sim -(\pi/H)^2(\chi, w)$. Thus, terms PA and WA are just proportional to the negative pressure tendency and the negative vertical velocity.

Term PB is proportional to the advection of absolute vorticity by the geostrophic flow. Term PC is attributed to the amplification or decay of midlatitude unstable waves. This term is called the differential density advection because of the hydrostatic equation $\partial p/\partial z = -\rho g$, or is called the thickness advection in the isobaric coordinate system as in Holton (1979, chap. 7). It tends to increase during a developing phase of a baroclinic wave and to decrease during a decaying phase of a baroclinic wave.

To estimate the terms on the right-hand side of the above two equations we chose a layer between 100 and 300 m, which represents the surface and the base of the front, respectively, with a center at 200 m. Figure 7 demonstrates the evolution of terms $-$PB and $-$PC for the flat-bottom run. As a baroclinic wave develops from day 20 to 40 (see also Fig. 2b), the advection of the absolute vorticity by the geostrophic flow increases (Fig. 7a). The absolute values between the high and low centers of PB are about 43, 113, and 143 (by a factor of $10^{-13}$) for days 20, 30, and 40, respectively. This indicates that the absolute vorticity gradually builds up and is advected by the geostrophic flow for a developing wave (see also Figs. 3a–b). On the other hand, the differential density advection ($-$PC, Fig. 7b) shows an evolution in thickness. The absolute values between the high and low centers of PC are about 44, 100, and 92 (by a factor of $10^{-13}$) for days 20, 30, and 40, respectively, with a peak value of 107 at day 39 (not shown). A physical interpretation is that during a developing phase of an unstable wave from day 20 to 39, the differential density advection (the thickness advection) increases, whereas during the decaying phase from day 39 on (see Fig. 2b), it decreases spatially (from 107 down to 92). The phase speed of the wave moving from west to east was estimated to be 7 cm s$^{-1}$ from day 20 to 35, based on the pressure tendency field [$-$(PB + PC), Fig. 7c].

As discussed earlier, with respect to the vertical velocity field (Fig. 3d), the ascending (descending) motion occurs to the west (east) of the surface high (ridge) in a developing wave. To reveal this phenomenon, we now examine the diagnostic equation of the vertical velocity. Equation (4) involves only derivatives in space. It is, therefore, a diagnostic equation for the $w$ field in terms of instantaneous pressure (i.e., density) and geostrophic flow fields. The $w$ equation, unlike the continuity equation, gives a measure of $w$ that does not depend on accurate observations of horizontal currents. Such velocity observations are now impossible to realize in the ocean. In the following, we make use of this method to reveal some interesting phenomena observed in Fig. 3d.

Term WB is called the differential vorticity advection, or the vertical difference between the upper (say, 100 m) and lower (say, 300 m) layer vorticity advection. It is proportional to the rate of increase with height of the advection of absolute vorticity. The evolution of term $-$WB for days 20, 30, and 40 at 200 m is shown in Fig. 8a. Note here that the positive sign stands for a positive vertical velocity (Fig. 3d) since term WA is proportional to $-w$ as discussed above, so that term $-$WB, as well as $-$WC, is proportional to positive w. The $-$WB field is similar to the model w field (Fig. 3d). This indicates a major contribution to the vertical velocity; that is, to the west (east) of a ridge, there is

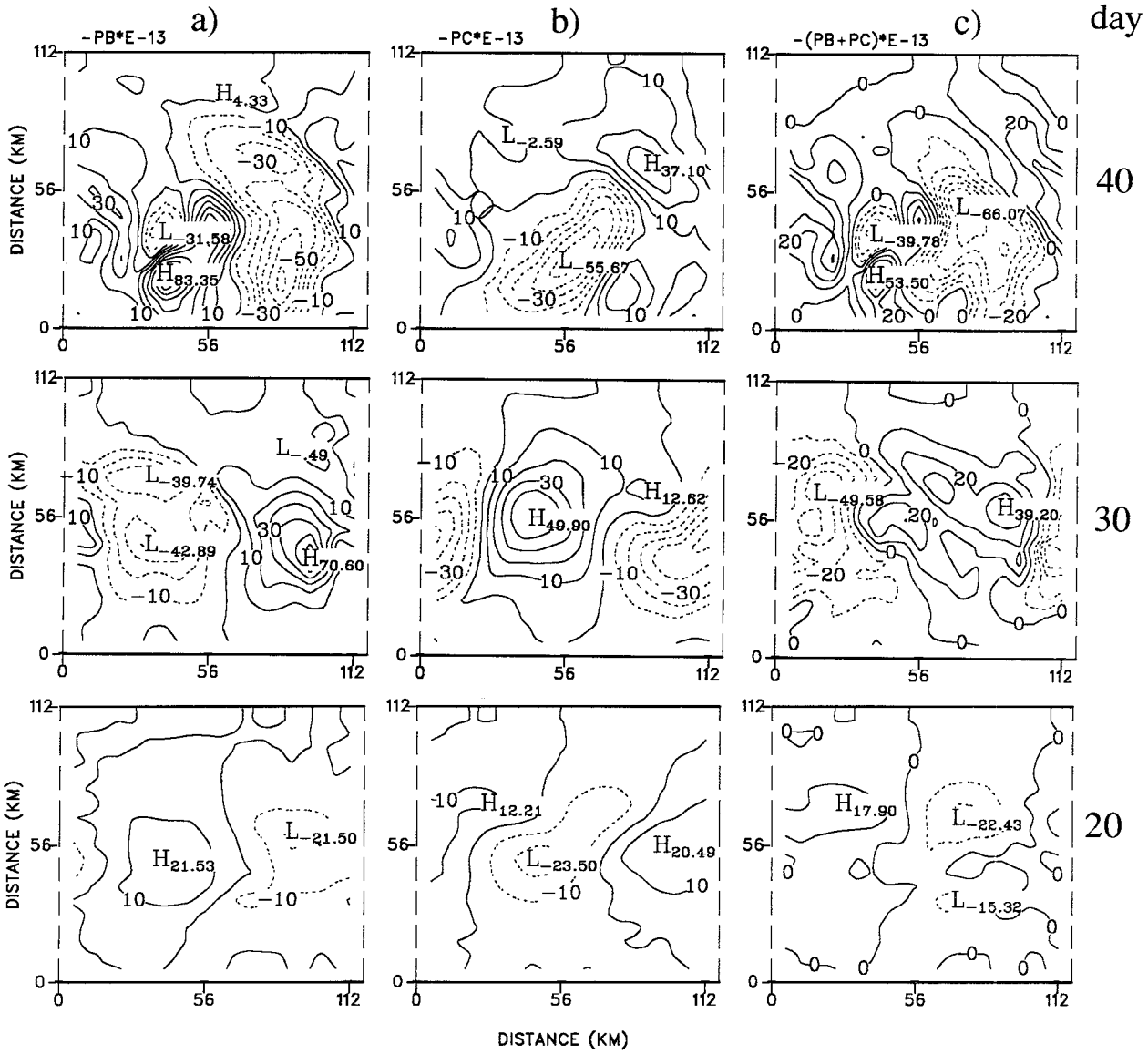


FIG. 7. Plan view of time sequences (day 20, 30, and 40) of terms (a) −PB, (b) −PC, and, (c) − (PB + PC) at 200-m depth in the pressure tendency equation. Contour interval is $10 \times 10^{-13}$ kg m$^{-3}$ s$^{-3}$. The positive (negative) values denote the positive (negative) pressure tendency, indicating pressure is increasing (decreasing).

positive (negative) differential vorticity advection, resulting in a positive (negative) vertical velocity at the center of the front (200 m in this case) due to the divergence (convergence) to the west (east) of the ridge in the layer.

Term WC is merely the negative of the horizontal Laplacian of the density advection, proportional to the density advection, since the Laplacian operator here leads to a negative sign. The plots of term −WC are shown in Fig. 8b. This term appears dominant on the smaller scales with comparable amplitude to term −WB. This term seems to be a ''sink or dissipation'' term because of the presence of the Laplacian of the density advection by the geostrophic flow. For example, as a wave is developing, this term continues increasing on small scales from day 20 to 40 caused by the density advection change. At day 40, one day after the wave starts to decay, these small-scale waves are more intense than day 30.

Vertical velocity field [−(WB + WC)] is obtained (Fig. 8c), which mimics the model vertical velocity pattern (Fig. 3d), except that −(WB + WC) slightly lags the model *w* field. Nevertheless, some small-scale features appear in Fig. 8c that are absent in Fig. 3d. This may clearly explain the cancellation between terms −WB and −WC, as Hoskins et al. (1978) pointed out. They found that the cancellation usually occurs in the calculation of terms WB and WC because both are as-

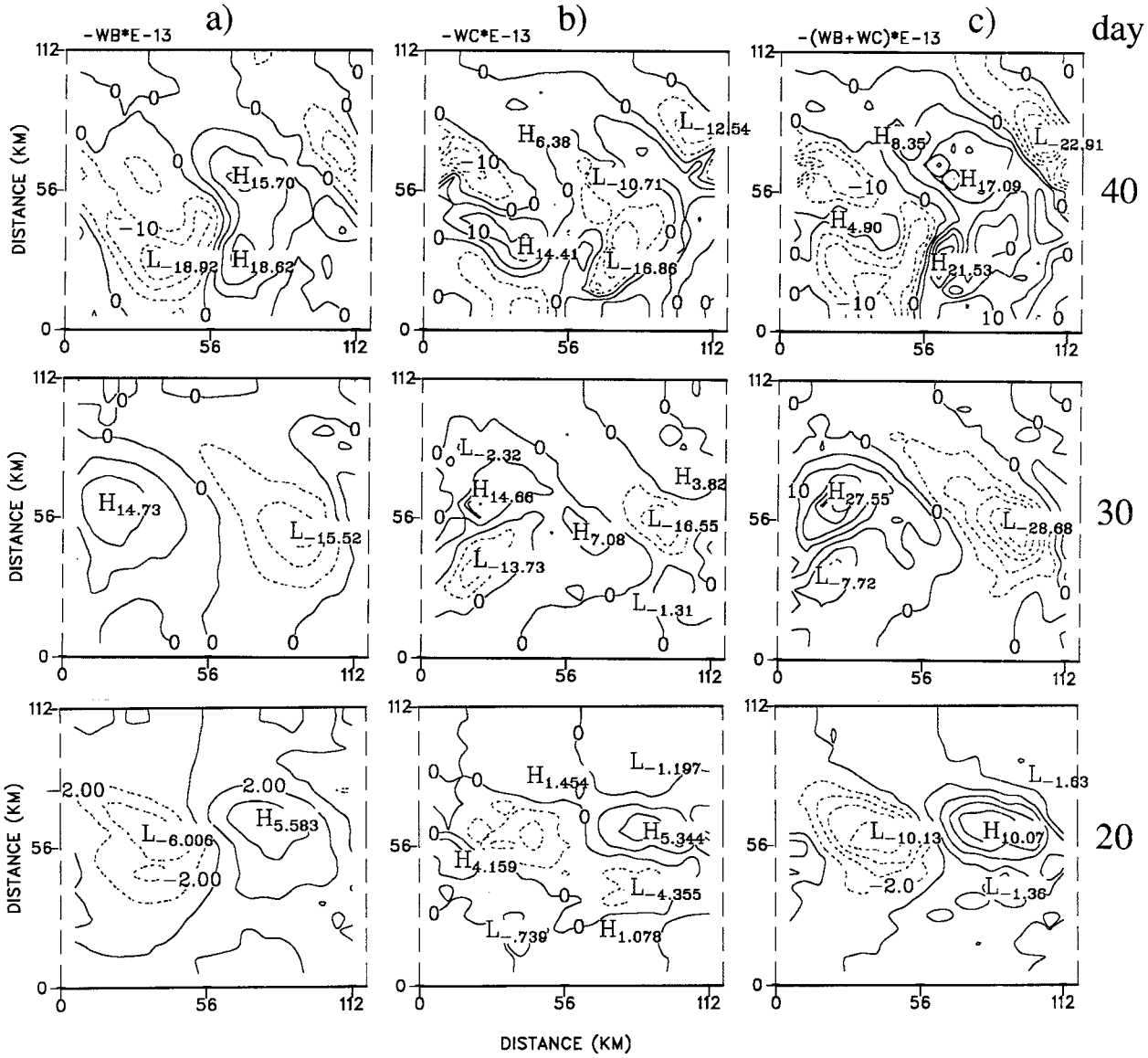


FIG. 8. Plan view of time sequences (days 20, 30, and 40) of terms (a) −WB, (b) −WC, and (c) −(WB + WC) at 200-m depth in the vertical velocity equation. Contour interval is $2 \times 10^{-13}$ m$^{-1}$ s$^{-1}$ for day 20 and $5 \times 10^{-13}$ m$^{-1}$ s$^{-1}$ for days 30 and 40. The positive (negative) values denote the upwelling (downwelling).

sociated with the differencing with respect to depth. For example, calculation of a quantity at 200-m depth requires quantities (or information) from both upper (100 m) and lower (300 m) layers, which are not in phase because of strong baroclinicity in nature. The other reason is that the vorticity advection (WB) and density advection (WC) are usually not in phase. The simple addition of these two terms will result in errors in phase and then in amplitude to the vertical velocity. Thus, the cancellation between these two terms is responsible for the numerical small-scale features or errors (Tintoré et al. 1991).

Comparing Figs. 7c and 8c, we observe that the region of positive (negative) vertical velocity corresponds to the negative (positive) pressure tendency; that is, the pressure tendency pattern and vertical velocity pattern are out of phase. This indicates that in the next time step the pressure will become lower (higher) in the region of positive (negative) vertical velocity; that is, a wave trough (ridge) will move to the region of positive (negative) vertical velocity at the present time.

### *b. Q-vector method*

To avoid the cancellation between terms WB and WC in the quasigeostrophic approach, we followed Hoskins et al. (1978) and Hoskins and Pedder (1980) and used a Q-vector method. The fundamental difference between

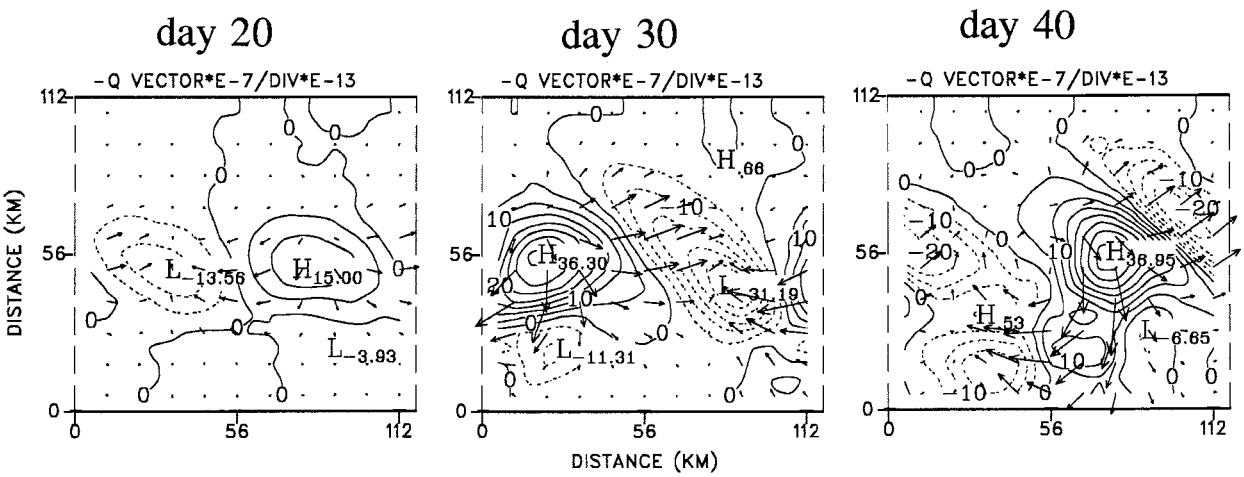


FIG. 9. Plan view of time sequences (days 20, 30, and 40) of $-2\nabla\cdot\mathbf{Q}/N^2$ superimposed by $-\mathbf{Q}$ vector at 200-m depth. Contour interval of $-2\nabla\cdot\mathbf{Q}/N^2$ is $5 \times 10^{-13}$ m$^{-1}$ s$^{-1}$ (as in Fig. 10). The maximum vector denotes $2 \times 10^{-7}$ s$^{-3}$. The positive (negative) values denote the upwelling (downwelling).

the QG and Q-vector methods is that the latter introduces an ageostrophic component that is neglected by the former (the detailed derivation and discussion of the equation have been given by Pollard and Regier 1992). Thus, the vertical velocity can be estimated from the following Q-vector equation:

$$\left(\nabla^2 + \frac{f_0^2}{N^2}\frac{\partial^2}{\partial z^2}\right)w = \frac{2}{N^2}\nabla\cdot\mathbf{Q}, \tag{5}$$

where

$$\mathbf{Q} = \frac{g}{\rho_0}\left(\frac{\partial u_g}{\partial x}\frac{\partial \rho}{\partial x} + \frac{\partial v_g}{\partial x}\frac{\partial \rho}{\partial y}, \frac{\partial u_g}{\partial y}\frac{\partial \rho}{\partial x} + \frac{\partial v_g}{\partial y}\frac{\partial \rho}{\partial y}\right). \tag{6}$$

The **Q** vector and its divergence can be calculated at depth of 200 m. Figure 9 shows the negative **Q** vector and its divergence, which corresponds to the positive (negative) vertical velocity when the values are positive (negative). It is obvious that the convergence corresponds to the downwelling, whereas the divergence to the upwelling. The comparison of the results between the quasigestrophic approach (Fig. 8c) and the Q-vector method (Fig. 9) indicates that the latter has no small-scale features that appear in the former due to the cancellation as discussed before (section 4a). Although the gross patterns are similar, the magnitude in Fig. 9 is slightly larger than that in Fig. 8c. The phase speeds in Figs. 8c and 9 are compared fairly well to each other, but both slightly lag the model *w* (Fig. 3d).

Comparing Q-vector-derived *w* and model *w*, we observe that before day 39, the similarity is high, while they are less similar to each other at day 40 than days 20 and 30. The reason is that after day 39, the baroclinic wave is in the decaying phase during which the dissipation term plays an important role in the voticity balance. Nevertheless, in the diagnostic equations, the dissipation terms are neglected. This may explain the larger discrepancy during the decaying phase. To verify this, the results at day 60 during the decaying (or stationary) phase (from day 50 to 60) are shown in Fig. 10. The ridge position (Fig. 10a) at day 60 is similar to that at day 50 (not shown), indicating a stationary phase; that is, the wave no longer propagates downstream. The vertical velocity derived from the Q-vector method (Fig. 10d) has some similarity to the model *w* (Fig. 10b), while the comparison is much poorer than that during the developing phase of the unstable wave. The QG method yields *w* with much noise (Fig. 10c) and cannot capture the model *w* field at all (Fig. 10b).

Therefore, it is recommended that the Q-vector method be widely used to estimate vertical velocity from a hydrographic CTD array more accurately during the developing phase of a baroclinic wave. During the decaying phase, this method should be used with caution because of the inviscid assumption.

## 5. Conclusions and discussion

Based on the above investigations, we summarize the findings as follows:

1) The modified version of the ECOMSI with the predictor–corrector scheme has a neutral amplification for inertial waves and is suitable for simulating the meander and unstable baroclinic waves in a low viscosity ocean. The Euler forward scheme with an explicit treatment of the Coriolis terms contains an unstable numerical mode and should be used carefully.
2) A propagation speed (6–7 cm s$^{-1}$) of the unstable baroclinic wave was estimated to be a few tens of percent of the mean flow speed. One important finding is that the upper-layer (frontal) wave lags the lower-layer wave by about 90 degrees, indicating a vertical shear (or tilting of trough and ridge lines) in a developing unstable wave. This finding is con-

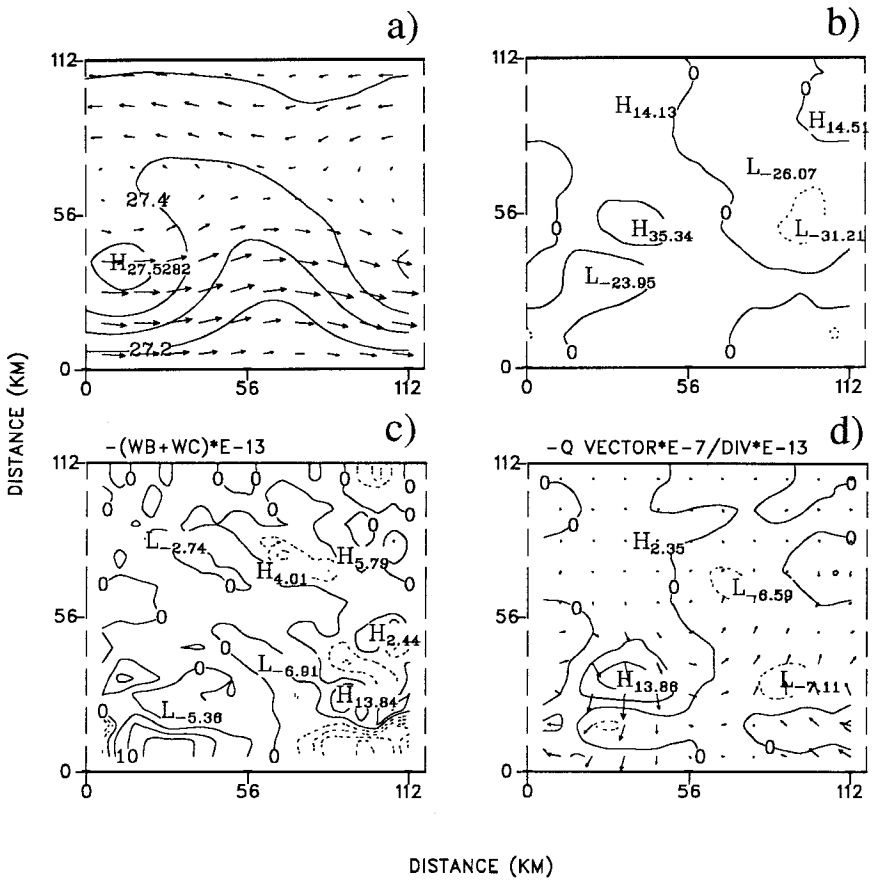


FIG. 10. Plan view at 200-m depth of sigma-t superimposed by (a) velocity field, (b) model vertical velocity, (c) $-$(WB + WC) from the QG method, and (d) Q-vector derived vertical velocity. Contour interval is 0.1 kg m$^{-3}$ for density (a), $25 \times 10^{-4}$ cm s$^{-1}$ for model $w$ (b), $5 \times 10^{-13}$ m$^{-1}$ s$^{-1}$ for QG-method-derived $w$ (c), and $5 \times 10^{-13}$ m$^{-1}$ s$^{-1}$ Q-vector-method-derived $w$ (d). Positive (negative) values denote the upwelling (downwelling).

sistent with the observations of synoptic baroclinic waves in the atmosphere (Holton 1979; Gill 1982), although no documentation of such tilt has been made for ocean mesoscale eddy measurements. However, this tilt has also been predicted in some previous models based on the phase information (Killworth et al. 1984; Wood and Ikeda 1994). One would expect the tilt to decrease as the meander develops. This property should be reflected in the horizontal velocity signals. Thus, this finding suggests that when a field survey is designed to detect the mesoscale eddy activity in the future, a mooring with a few current meters at different depths should be deployed (at least one at the surface of the front and the other at the base of the front) around or downstream of the center of the eddy.

3) A gentle positive slope bottom deters the baroclinic waves from developing, whereas a gentle negative slope favors unstable wave development in this configuration. Thus, the continental slope along the east coast of North America usually deters the development of baroclinic waves. However, away from the continental slope off the New England coast (about 40°N) (Richardson 1981), the topographic effects are weak, as the development of the Gulf Stream meanders and mesoscale eddies have been observed.
4) When the negative slope is introduced, the linear growth rate of the unstable wave tends to shift toward higher wavenumber (shorter wavelength). The steeper the negative slope, the more the growth rate is reduced.
5) Two QG diagnostic equations, one for pressure tendency and the other for vertical velocity, were derived to reveal the dynamic processes in a developing wave. The diagnostic analysis for the pressure tendency indicates that both absolute vorticity advection and the differential density advection (or thickness) in the front contribute to a developing wave. As the wave develops, the differential density advection (thickness) increases; whereas during a decaying phase, the differential density advection (thickness) decreases.
6) The distribution of vertical velocity can be sketched in Fig. 11: to the west (east) of the surface ridge,

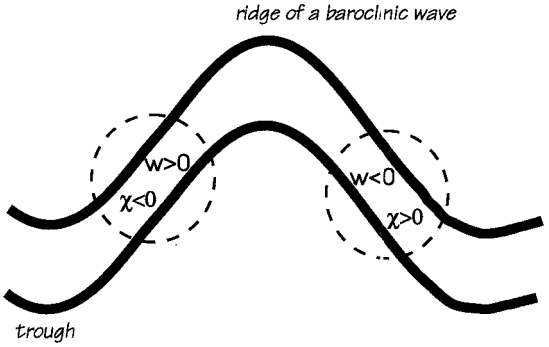


FIG. 11. Schematic diagram of instantaneous spatial distribution of vertical velocity at 200-m depth during a developing phase of a baroclinic wave. Upwelling (downwelling) and negative (positive) pressure tendency occur to the west (east) of the wave ridge.

upwelling (downwelling) occurs as the wave moves downstream and grows. However, during a mature or decaying phase of the baroclinic wave (or a detached eddy), the upwelling (downwelling) occurs simultaneously in the wave ridge (trough), or in the higher (lower) center. This finding is consistent with the result by Bower and Rossby (1989, their Fig. 5). The major mechanism is the differential absolute vorticity advection in the front, that is, the rate of increase of the absolute vorticity advection with height, based on the quasigeostrophic approach. The Q-vector method was also applied to demonstrate the vertical velocity pattern with slightly larger amplitude than that obtained from the quasigeostrophic approach. The $w$ field derived from both QG and Q-vector methods slightly lags the model output $w$. The mechanism responsible for this lag is not clear.

In summary, the advantage of the Q-vector method is that there is no cancellation that is observed in the quasigeostrophic approach. Thus, the Q-vector method should be widely used to estimate vertical velocity from hydrographic data collected in a period of a few days. The vertical velocity estimated from this method is more accurate during the developing phase than during the decaying or stationary phase of the baroclinic wave.

*Acknowledgments.* JW appreciates the support mainly from the Federal Panel on Energy Research and Development through the NSERC of Canada Visiting Postdoctoral Fellowship, which was held at the Bedford Institute of Oceanography (95%), and partly from USCG and NOAA to the Ocean Pollution Research Center at University of Miami (5%). We thank A. van der Baaren for assistance with some figures and comments on a draft of this paper. We also thank Prof. J. Gyakum for his comments on this paper, and Drs. C. Griffiths and P. C. Smith for their fruitful discussions of the mesoscale dynamics during the course of this study. The authors thank two anonymous reviewers for their very constructive comments on this paper.

## REFERENCES

Asselin, R., 1972: Frequency filter for time integrations. *Mon. Wea. Rev.*, **100,** 487–490.

Blumberg, A. F., 1991: A primer for ECOM-si. Technical Report for HydroQual, Inc., Mahwah, NJ, 66 pp.

Boudra, D. B., R. Bleck, and F. Schott, 1988: A numerical model of instabilities in the Florida Current. *J. Mar. Res.*, **46,** 715–751.

Bower, A. S., and T. Rossby, 1989: Evidence of cross-frontal exchange processes in the Gulf Stream based on isopycnal RAFOS float data. *J. Phys. Oceanogr.*, **19,** 1177–1190.

Casulli, V., and R. T. Cheng, 1992: Semi-implicit finite-difference methods for three-dimensional shallow water flow. *Int. J. Numer. Methods Fluids*, **15,** 629–648.

Chao, S.-Y., 1990: Instabilities of fronts over a continental margin. *J. Geophys. Res.*, **95,** 3199–3211.

Cox, M. D., 1984: A primitive equation, three-dimensional model of the ocean. GFDL Ocean Group Tech. Rep. No. 1.

Fofonoff, N. P., 1962: Physical properties of sea water. *The Sea*, Vol. 1, Wiley-Interscience, 3–30.

Gill, A. E., 1982: *Atmosphere–Ocean Dynamics.* Academic Press, 662 pp.

Griffiths, C., M. Ikeda, J. Wang, and P. C. Smith, 1997: A model comparison of simulating ocean mesocale eddies in the presence of topography. *J. Phys. Oceanogr.*

Holland, W. R., 1978: The role of mesoscale eddies in the general circulation of the ocean—Numerical experiments using a wind-driven quasi-geostrophic model. *J. Phys. Oceanogr.*, **8,** 363–392.

Holton, J. R., 1979: *An Introduction to Dynamic Meteorology.* Academic Press, 391 pp.

Hoskins, B. J., and M. A. Pedder, 1980: The diagnosis of middle latitude synoptic development. *Quart. J. Roy. Meteor. Soc.*, **106,** 707–719.

——, I. Draghici, and H. C. Davies, 1978: A new look at the $\omega$-equation. *Quart. J. Roy. Meteor. Soc.*, **104,** 31–38.

Ikeda, M., 1981: Meanders and detached eddies of a strong eastward-flowing jet using a two-layer quasi-geostrophic model. *J. Phys. Oceanogr.*, **11,** 526–540.

——, 1991: Mesoscale eddy formation and evolution in the ice-covered ocean. *Ann. Glaciol.*, **15,** 139–147.

——, and J. R. Apel, 1981: Mesoscale eddies from spatially growing meanders in an eastward-flowing oceanic jet using a two-layer quasi-geostrophic model. *J. Phys. Oceanogr.*, **11,** 1638–1661.

——, and L.-Q. Zhang, 1992: Mesoscale stability of an ocean current over the continental slope in the Bryan–Cox primitive equation model. *J. Mar. Syst.*, **3,** 519–527.

——, and R. A. Wood, 1993: Mesoscale stability of an ocean current in the Bryan–Cox model. *J. Geophys. Res.*, **98,** 12 527–12 536.

Joyce, T. M., 1984: Velocity and hydrographic structure of a Gulf Stream warm-core ring. *J. Phys. Oceanogr.*, **14,** 936–947.

Killworth, P. D., N. Paldor, and M. E. Stern, 1984: Wave propagation and growth on a surface front in a two-layer geostrophic current. *J. Mar. Res.*, **42,** 761–785.

Leach, H., 1987: The diagnosis of synoptic-scale vertical motion in the seasonal thermocline. *Deep-Sea Res.*, **34,** 2005–2017.

LeBlond, P. H., 1982: Satellite observations of Labrador current undulations. *Atmos.–Ocean*, **20,** 129–142.

Lee, T. N., and A. Mayer, 1977: Low-frequency current variability and spin off eddies on the shelf off southeast Florida. *J. Mar. Res.*, **35,** 193–220.

Lindstrom, S. S., and D. R. Watts, 1994: Vertical motion in the Gulf Stream near 68°W. *J. Phys. Oceanogr.*, **24,** 2321–2332.

Mellor, G. L., 1991: Users guide for a three-dimensional, primitive equation, numerical ocean model. Atmospheric and Oceanic Sciences Program, Princeton University, 39 pp.

——, and T. Yamada, 1982: Development of a turbulence closure model for geophysical fluid problem. *Rev. Geophys. Space Phys.*, **20,** 851–875.

Oey, L.-T., 1988: A model of Gulf Stream frontal instabilities, me-

anders and eddies along the continental slope. *J. Phys. Oceanogr.*, **18,** 211–229.
Orlanski, I., and M. D. Cox, 1973: Baroclinic instability in ocean currents. *Geophys. Fluid Dyn.*, **4,** 297–332.
Pollard, R. T., and L. A. Regier, 1992: Vorticity and vertical circulation at an ocean front. *J. Phys. Oceanogr.*, **22,** 609–625.
Richardson, P. L., 1981: Gulf Stream trajectories measured with free-drifting buoys. *J. Phys. Oceanogr.*, **11,** 999–1010.
Roache, P. J., 1976: *Computational Fluid Dynamics.* Hermosa, 446 pp.
Smogorinsky, J., 1963: General circulation experiments with the primitive equations. I. The basic experiment. *Mon. Wea. Rev.*, **91,** 99–164.
Spall, M. A., and A. R. Robinson, 1990: Regional primitive equation studies of the Gulf Stream meander and ring formation region. *J. Phys. Oceanogr.*, **20,** 985–1016.
Tintoré, J., D. Comis, S. Alonso, and G. Parrilla, 1991: Mesocale dynamics and vertical motion in the Alborán Sea. *J. Phys. Oceanogr.*, **21,** 811–823.
Vastano, A. C., J. E. Schmitz, and D. E. Hagan, 1980: The physical oceanography of two rings observed by the Cyclonic Ring Experiment. Part I: Physical structures. *J. Phys. Oceanogr.*, **10,** 493–513.
Wang, J., 1996: Global linear of the two-dimensional stability shallow-water equations: An application of the distributive theorem of roots for polynomials in the unit circle. *Mon. Wea. Rev.*, **124,** 1301– 1310.
——, and M. Ikeda, 1995: Stability analysis of finite difference schemes for inertial oscillations in ocean general circulation models. *Computer Modeling of Seas and Coastal Regions*, C. A. Brebbia and Coeditors, Computational Mechanics Publications, 19–27.
——, and ——, 1997: Inertial stability and phase error of time integration schemes in ocean general circulation models. *Mon. Wea. Rev.*, in press.
——, L. A. Mysak, and R. G. Ingram, 1994: A three-dimensional numerical simulation of Hudson Bay summer circulation: Topographic gyres, separations, and coastal jets. *J. Phys. Oceanogr.*, **24,** 2496–2514.
Wood, R. A., 1988: Unstable waves on oceanic fronts: Large amplitude behavior and mean flow generation. *J. Phys. Oceanogr.*, **18,** 775–787.
——, and M. Ikeda, 1994: Comparison of mesoscale meanders and eddies simulated by quasi-geostrophic and primitive equation models: A case study. *J. Geophys. Res.*, **99,** 22 645–22 663.